Schweizerischer Erdbebendienst
Service Sismologique Suisse
Servizio Sismico Svizzero
Swiss Seismological Service

ETH zürich

SITE CHARACTERIZATION REPORT

SEFS: Erstfeld (UR) - Schule

Manuel Hobiger, Donat Fäh

Last Modification: 25th February, 2020

Schweizerischer Erdbebendienst (SED)
Service Sismologique Suisse
Servizio Sismico Svizzero
Servizi da Terratrembels Svizzer

ETH Zürich
Sonneggstrasse 5
8092 Zürich
Schweiz
manuel.hobiger@sed.ethz.ch

Contents

Summary

The free-field strong-motion station SEFS was built in vicinity of the Schulhaus Jagdmatt in Erstfeld (UR). We performed a passive seismic array measurement to characterize the site, which is located in the alluvial valley of the Reuss river.
The array measurements were analyzed with different techniques, namely 3-component HRFK, WaveDec and SPAC. All techniques gave similar dispersion curves. For Love waves, the dispersion curves for the fundamental and a higher mode were retrieved. For Rayleigh waves, the dispersion curves for the fundamental and a higher mode were identified. The measured H/V and ellipticity curves show clear signs of a two-dimensional valley resonance. The polarization analysis supports this and indicates a fundamental frequency of about 0.55 Hz. Using the array recordings, we can identify the fundamental mode of the valley resonance at about 0.56 Hz and can identify other modes, too. For a more thorough determination of the eigenmodes in the valley, a more detailed measurement along a profile crossing the whole valley would need to be performed.
The joint inversion of the Love and Rayleigh wave dispersion curves yields structures which can be be summarily explained by a first layer with a thickness of 6 m and an S-wave velocity of about 275 m/s, followed by a layer with a velocity of 395 m/s down to about 16 m, where the velocity increases to about 448 m/s. The bedrock cannot be retrieved. The V_{S30} of the best models is about 383 m/s, corresponding to soil class B in EC8 and C in SIA261.

1 Introduction

In the framework of the second phase of the Swiss Strong Motion Network (SSMNet) renewal project, a new station was planned to be installed in Erstfeld (UR). The final location of the station was selected in vicinity to the school building of Jagdmatt. The new station, called SEFS, went operational on 13 July 2017. The location of the station is shown in Fig. 1.

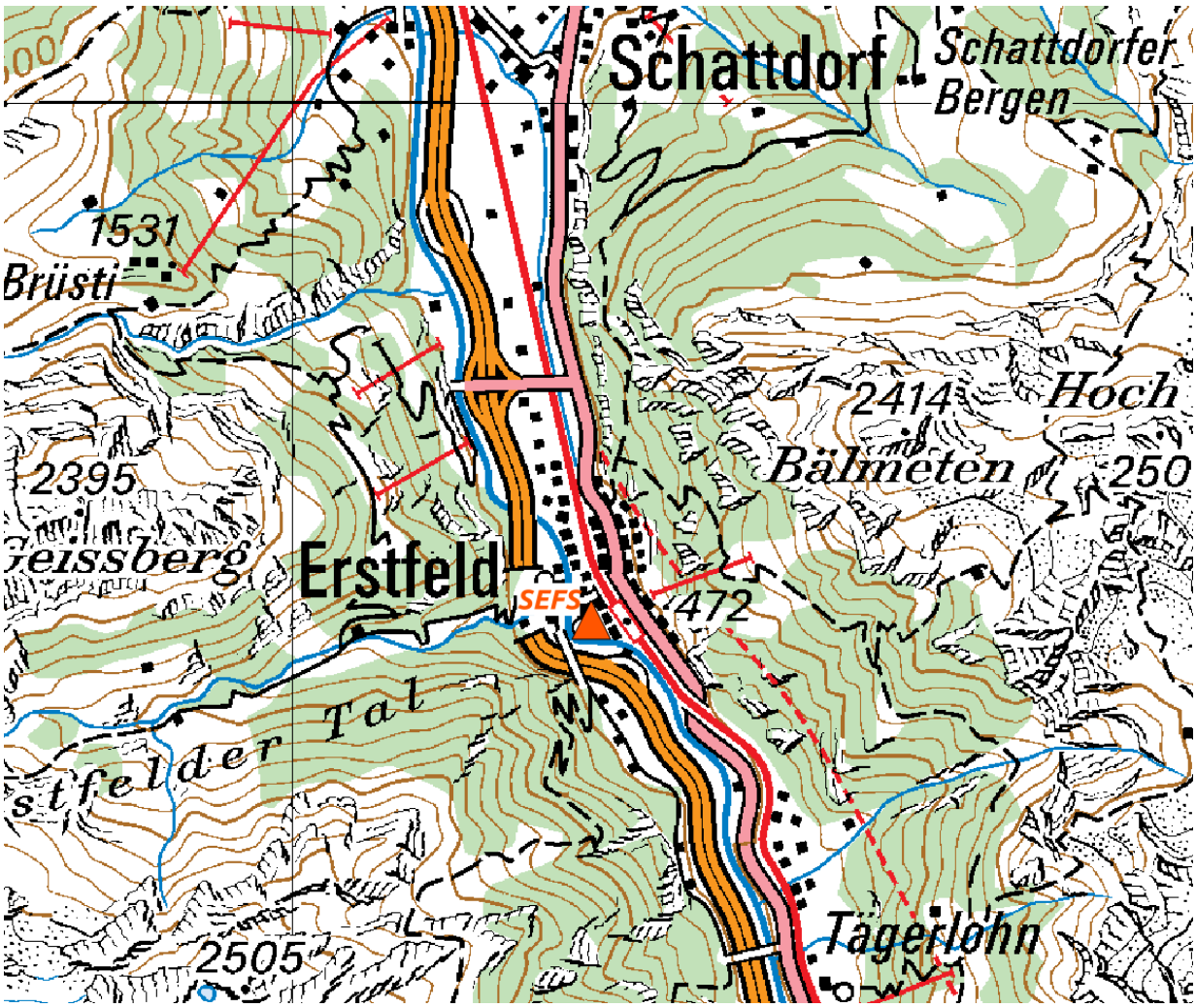

Figure 1: Map showing the location of station SEFS in Erstfeld.

2 Geological setting

A geological map of the surroundings of station SEFS is shown in Fig. 2. The station is located on alluvial deposits in the narrow Alpine valley of the Reuss.

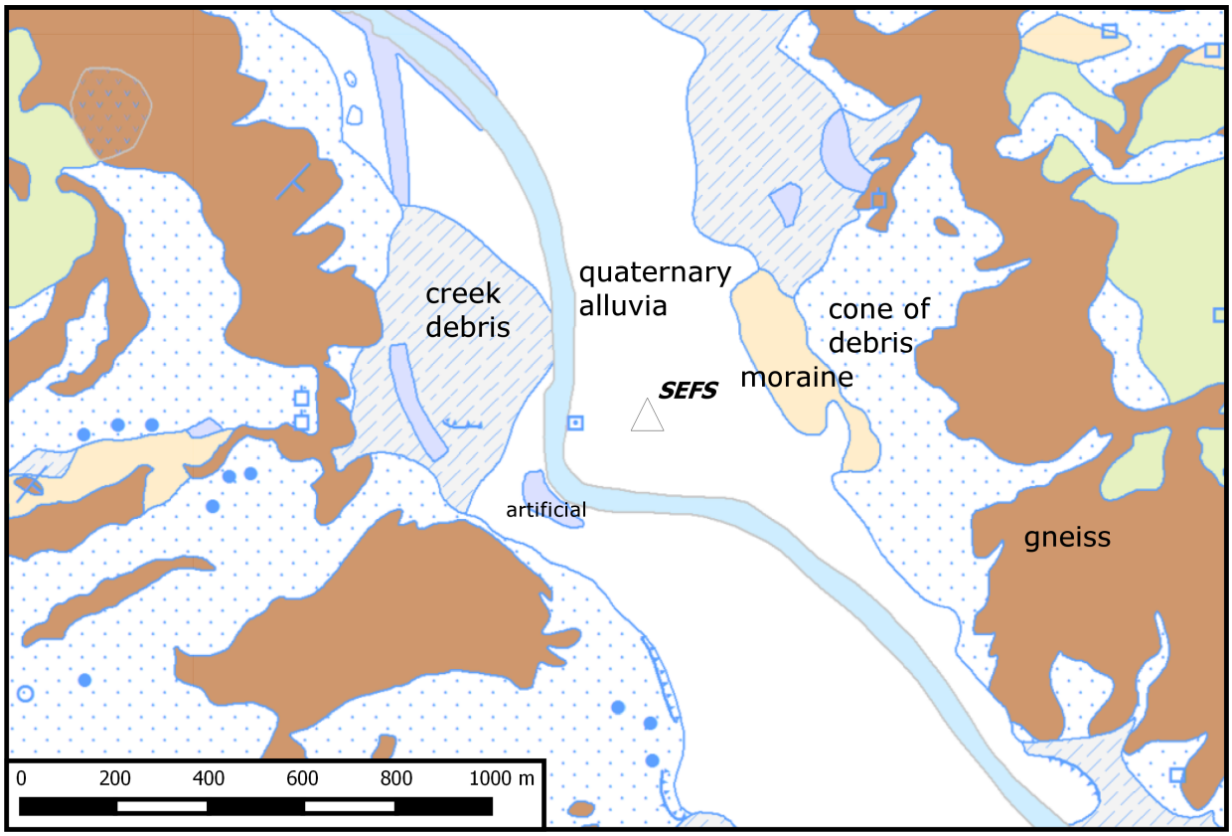

Figure 2: Geological map of the area around station SEFS. According to the geological atlas, station SEFS and all stations of the passive array measurement lie on alluvial deposits.

3 Site characterization measurements

3.1 Data set

In order to characterize the local underground structure around station SEFS, passive seismic array measurements were carried out on 10 October 2017. The layout of the seismic array is shown in Fig. 3.
A single array of 16 stations was installed. The stations were planned to be located on five rings around a central station (called SEFS69). The radii of the respective rings were planned to be 5, 15, 33, 75 and 110 m, respectively. The stations were planned to be installed regularly on the different rings, i.e. with an angular distance of 120° from each other. Due to space constraints, the stations of the two inner rings were located in a line, when seen from the central station. The outer rings were rotated with respect to the inner ones.
Each installed station consisted of a Lennartz 5s sensor connected to a Centaur digitizer, where four stations in the central part had two sensors connected to the same digitizer. The station names of the array are composed of "SEFS" followed by a two-digit number between 42 and 49, 52 and 55, 62, 65, 69 and 72 (corresponding to the Centaur digitizer serial number for numbers lower than 60 and serial number plus 20 for higher numbers, i.e. the B channels of the Centaur). The minimum and maximum inter-station distances in the array were 4.9 m and 204.6 m, respectively. The array recording time was 160 minutes (9600 s). An additional seismic station, called ERS101 (see location in Fig. 3), was installed next to the permanent station SEFS during the dismantling of the seismic array in order to measure an H/V curve next to this station.
The station locations have been measured by a differential GPS system (Leica Viva GS10) which was set up to measure with a precision better than 5 cm. This precision was achieved for all stations.

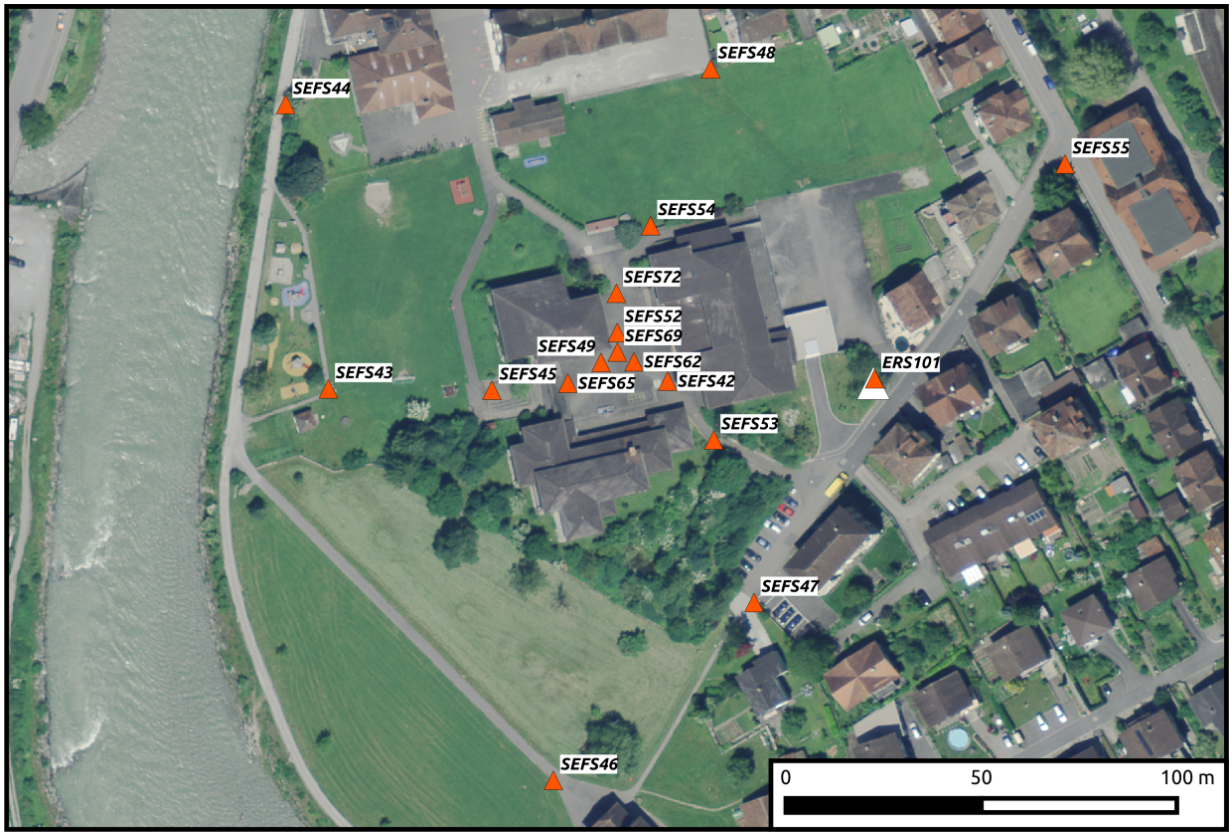

Figure 3: Layout of the array measurements around station SEFS. The location of SEFS is indicated by the white triangle next to station ERS101, the locations of the stations for the passive seismic measurement by the orange triangles. ©2018 swisstopo (JD100042)

3.2 H/V curves

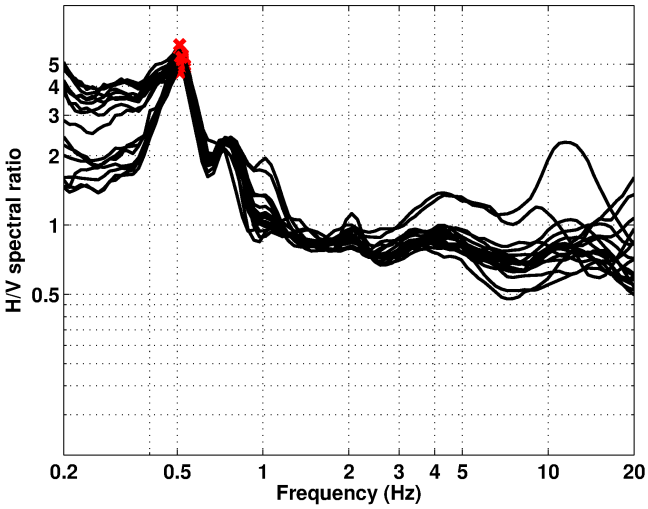

Figure 4: Overview of the H/V measurements for the different stations of the array measurement in Erstfeld.

Figure 4 shows the H/V curves determined with the time-frequency analysis method (Fäh et al., 2009) for all stations of the passive array. All curves show the same fundamental frequency, which is determined as 0.52 Hz and not much variability in the higher frequency range. A possible reason for this behavior might be a very homogeneous lithology with a constant thickness of the sedimentary layers below the array and prevailing 1-dimensional resonance. Another explanation are 2- or 3-dimensional resonance effects which lead to a synchronized vibration of the whole valley. This topic will be investigated more in detail later in this report. Two stations, SEFS43 and SEFS44, show higher H/V ratios than the other stations at frequencies above 3 Hz, probably caused by a changes of the surficial structure below these stations, which are located closer to the river.

3.3 RayDec ellipticity curves

The RayDec technique (Hobiger et al., 2009) is meant to eliminate the contributions of other wave types than Rayleigh waves and give a better estimate of the ellipticity than the classical H/V technique. The RayDec ellipticity curves for all stations of the array measurements are shown in Fig. 5 and are very similar to the H/V curves.

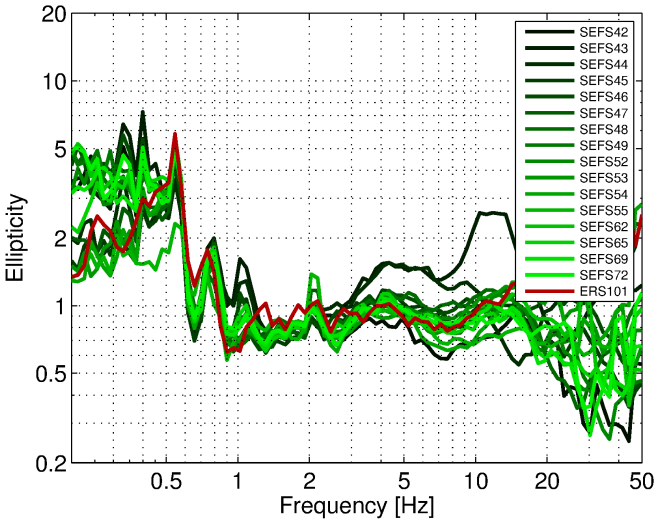

Figure 5: RayDec ellipticities for all stations of the array. The curve of ERS101, closest to the permanent station SEFS, is highlighted in red.

3.4 Polarization measurements

The polarization analysis was performed according to Burjánek et al. (2010) and Burjánek et al. (2012). The results for all stations of the array are similar. The results for station ERS101 next to SEFS are shown in Fig. 6. We clearly see that the particle motion is linear at a frequency determined here as 0.55 Hz and is oriented along the 150° - 330° axis with respect to the north, i.e. along the valley axis. We conclude that the 2-dimensional polarization effects clearly dominate the particle motion at the fundamental frequency. The eigenmodes of the 2-dimensional valley polarization will be investigated more in detail in section 5.

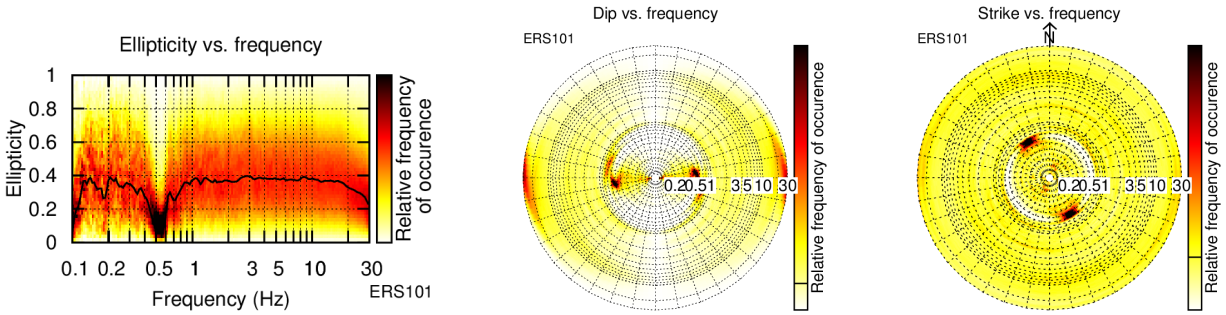

Figure 6: Polarization analysis of station ERS101.

3.5 3-component high-resolution FK

The results of the 3-component high-resolution FK analysis (Poggi and Fäh, 2010) are shown in Fig. 7. On the transverse component, we can identify the dispersion curves for the fundamental mode and a higher mode of Love waves. The fundamental mode is better resolved and can be picked between 1.9 and 42.1 Hz. The higher mode is not very clearly resolved and can be picked between 6.7 and 40.0 Hz.
On the vertical component, two modes are clearly visible. The fundamental mode can be picked between 1.4 and 36.3 Hz, a higher mode between 5.2 and 17.3 Hz. The corresponding result on the radial component is worse and does not allow us to pick any dispersion curve.
The ellipticity curves of the modes picked on the vertical component are rather flat and do not show pronounced peaks in the respective frequency ranges.

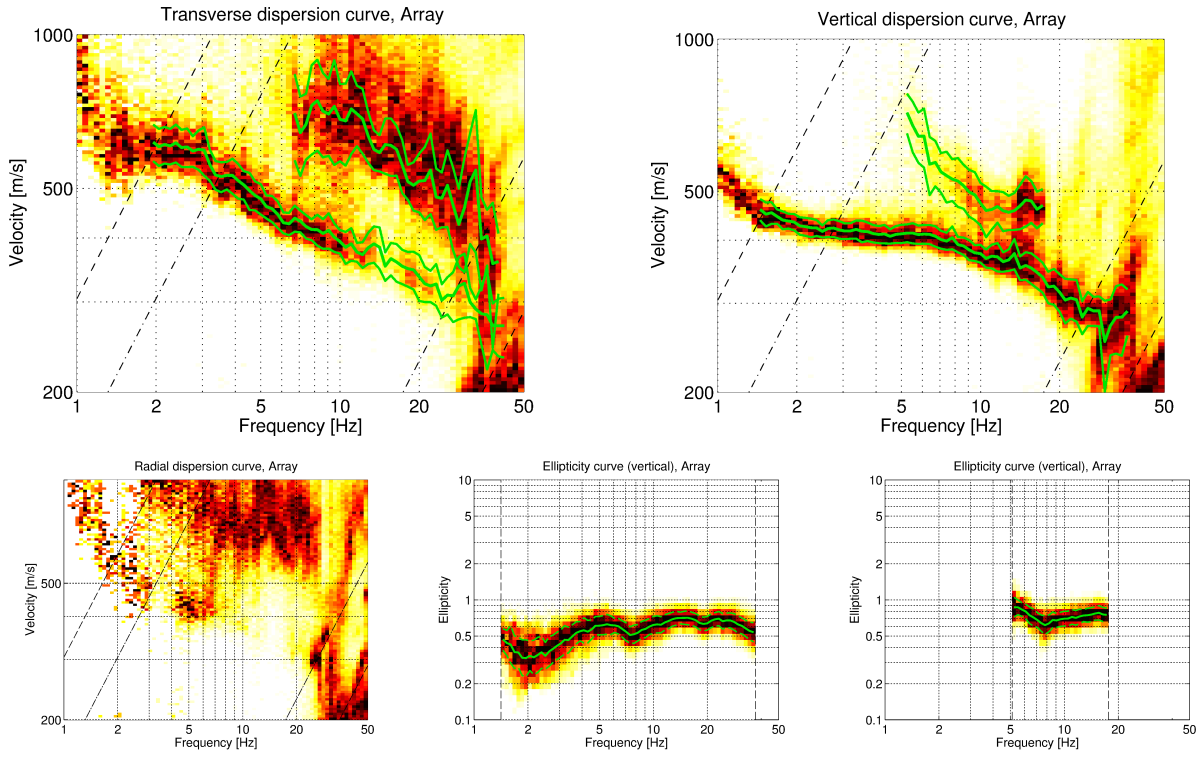

Figure 7: Dispersion and ellipticity curves obtained with the 3-component HRFK algorithm (Poggi and Fäh, 2010). The dispersion curves for the transverse, vertical and radial components are shown, as well as the ellipticity curves for the two modes picked on the vertical and the radial component. The dashed and dash-dotted black lines are the array resolution limits for high-resolution and classical FK analysis, respectively. The solid green lines are picked from the data, where the central line indicates the best values and the two outer lines the standard deviation.

3.6 WaveDec

The results of the WaveDec (Maranò et al., 2012) processing are shown in Fig. 8. This technique estimates the properties of single or multiple waves simultaneously with a maximum likelihood approach. In order to get good results, the parameter γ has been tuned to modify the sharpness of the wave property estimation between purely maximum likelihood estimation and a Bayesian Information Criterion. Here, a value of $\gamma = 0.2$ was used, i.e. the estimation follows mainly the maximum likelihood approach. The dispersion curve of the fundamental Love wave mode is retrieved between 2.3 and 23.4 Hz. The mode is less resolved than using the high-resolution FK analysis and no higher mode can be identified. The Rayleigh wave dispersion curve of the fundamental mode can be picked between 2.7 and 14.5 Hz. The ellipticity angle for the picked Rayleigh wave dispersion curve is negative in this whole frequency range, corresponding to retrograde particle motion. The ellipticity curve obtained by calculating the tangent of the absolute value of the ellipticity angle results in a rather flat curve without pronounced peaks.

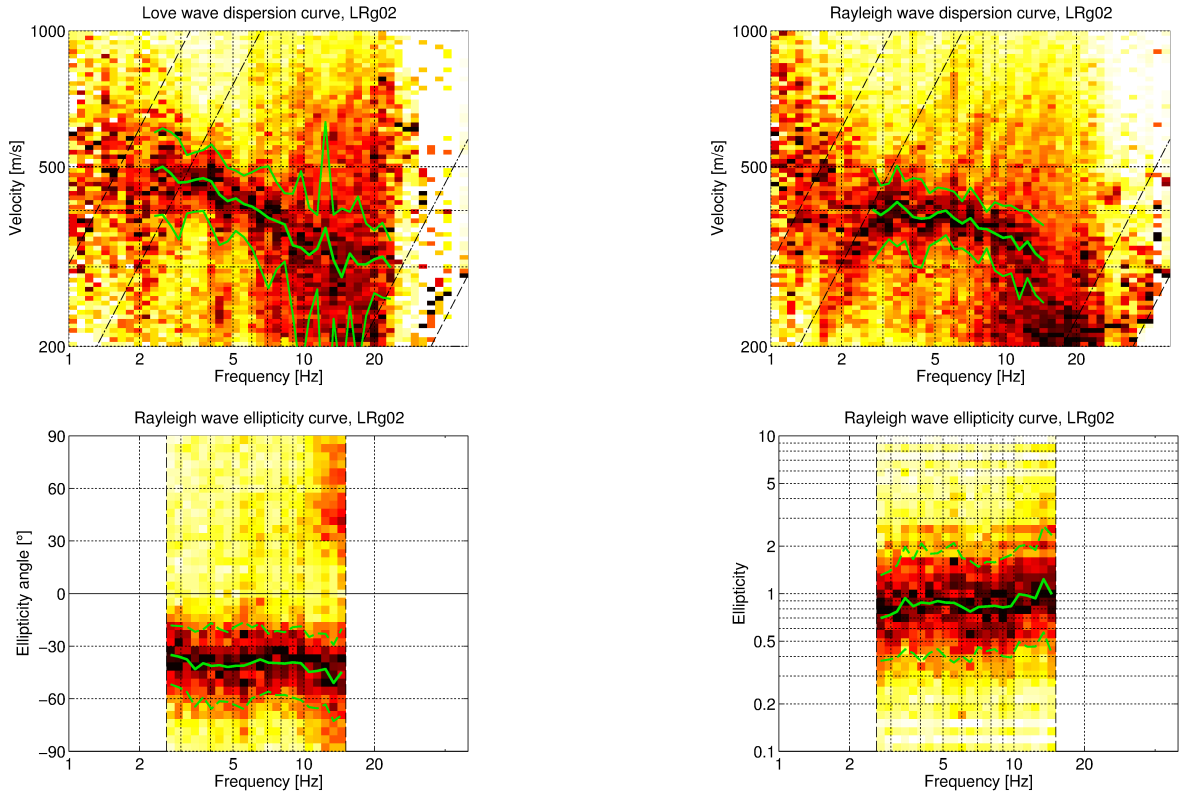

Figure 8: Love and Rayleigh wave dispersion (top) and ellipticity (bottom) curves obtained with the WaveDec technique (Maranò et al., 2012). The dashed and dash-dotted lines indicate the same theoretical array resolution limits as in Fig. 7.

3.7 SPAC

The SPAC (Aki, 1957) curves of the vertical components have been calculated using the M-SPAC (Bettig et al., 2001) technique implemented in geopsy. Rings with different radius ranges had been defined previously and for all station pairs with distance inside this radius range, the cross-correlation was calculated at different frequencies. These cross-correlation curves are averaged for all station pairs of the respective ring and give the SPAC curves. The rings are defined in such a way that at least three station pairs contribute and that their connecting vectors have a good directional coverage.
The dispersion curve shown in Fig. 9 has been obtained using the function `spac2disp` of the geopsy package. The SPAC curves for all defined rings are shown in Fig. 10, where the black dots indicate the data values which contributed to the final dispersion curve estimation.
The SPAC curves for all rings are of good quality and very similar to the Bessel functions which should be obtained theoretically. Using SPAC, we can pick a Rayleigh wave dispersion curve between 0.75 and 25.4 Hz.

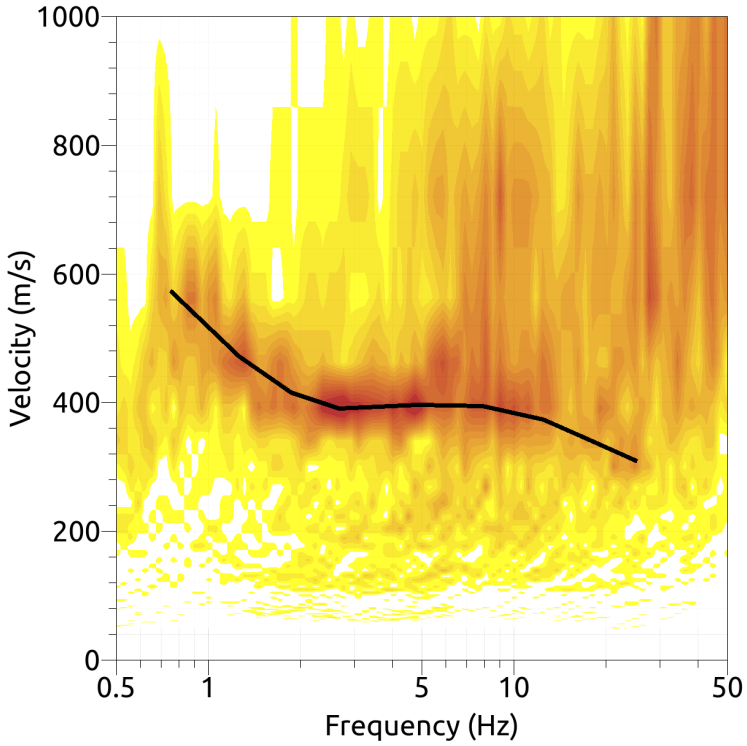

Figure 9: Resulting Rayleigh wave velocities. The black line corresponds to the picked dispersion curve.

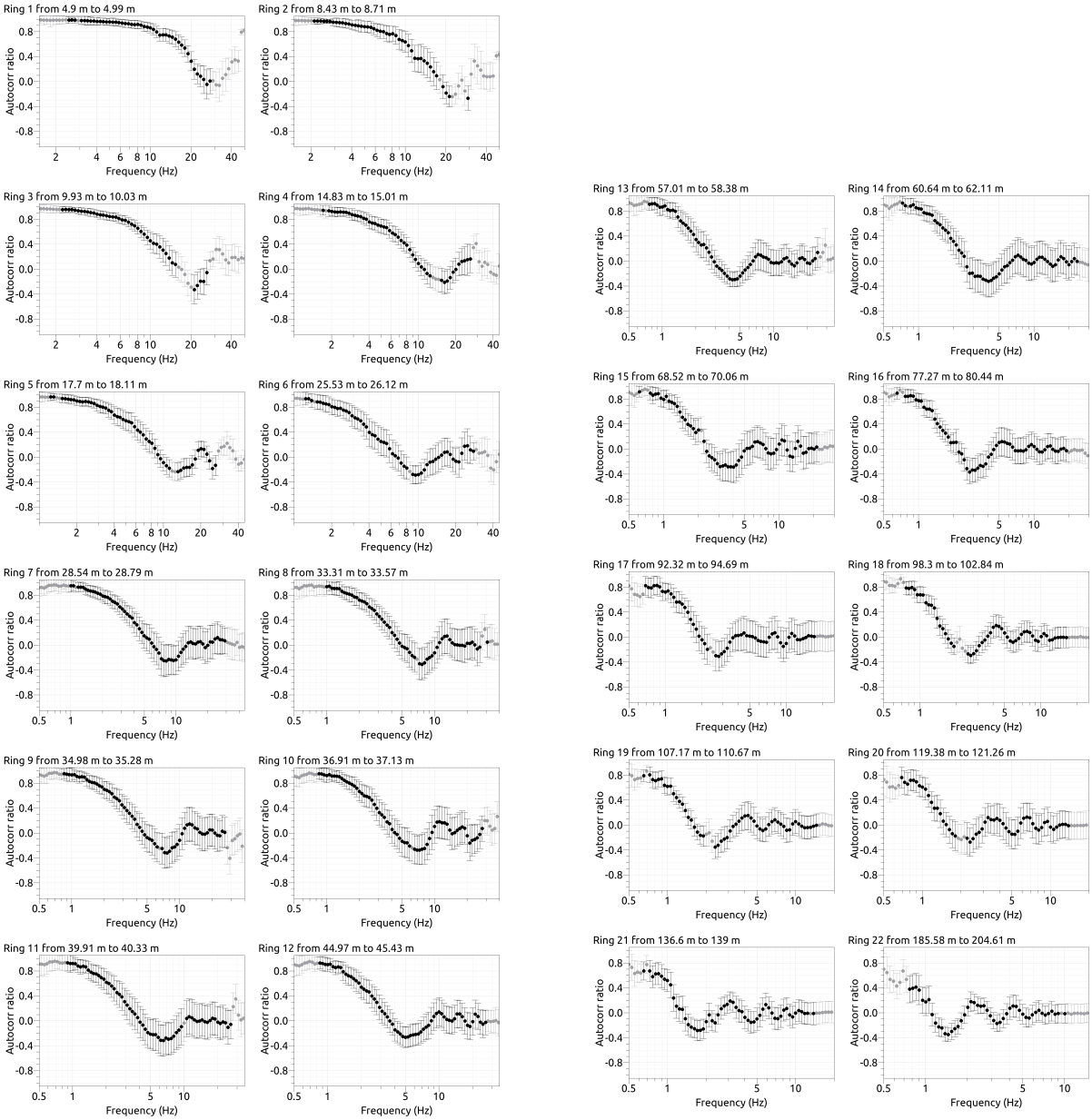

Figure 10: SPAC curves. The black data points contributed to the dispersion curve estimation.

3.8 Summary

Fig. 11 gives an overview of the dispersion and ellipticity curves determined by the different methods.
For Love waves, the HRFK and WaveDec results for the fundamental mode are similar, but differ. Taking the scatter of the WaveDec curve into consideration, both curves are still in agreement. The higher mode was only visible with HRFK, but as it was badly resolved, its composition is unclear.
For the Rayleigh waves, all curves are in very good agreement. Also here, the harmonic mode is only visible using HRFK.
The ellipticity curves retrieved using the different methods are also in agreement. The low frequencies of the fundamental peak can only be retrieved using single-station methods, such as RayDec. In the frequency range resolved by WaveDec, this method is in very good agreement with RayDec. The HRFK curves are lower than the RayDec and WaveDec curves. The fundamental ellipticity peak was identified to be caused by the 2-dimensional resonance of the whole valley and does therefore not correspond to the ellipticity of the Rayleigh waves at these frequencies. Therefore, it will not be used in the inversion for the underground structure.

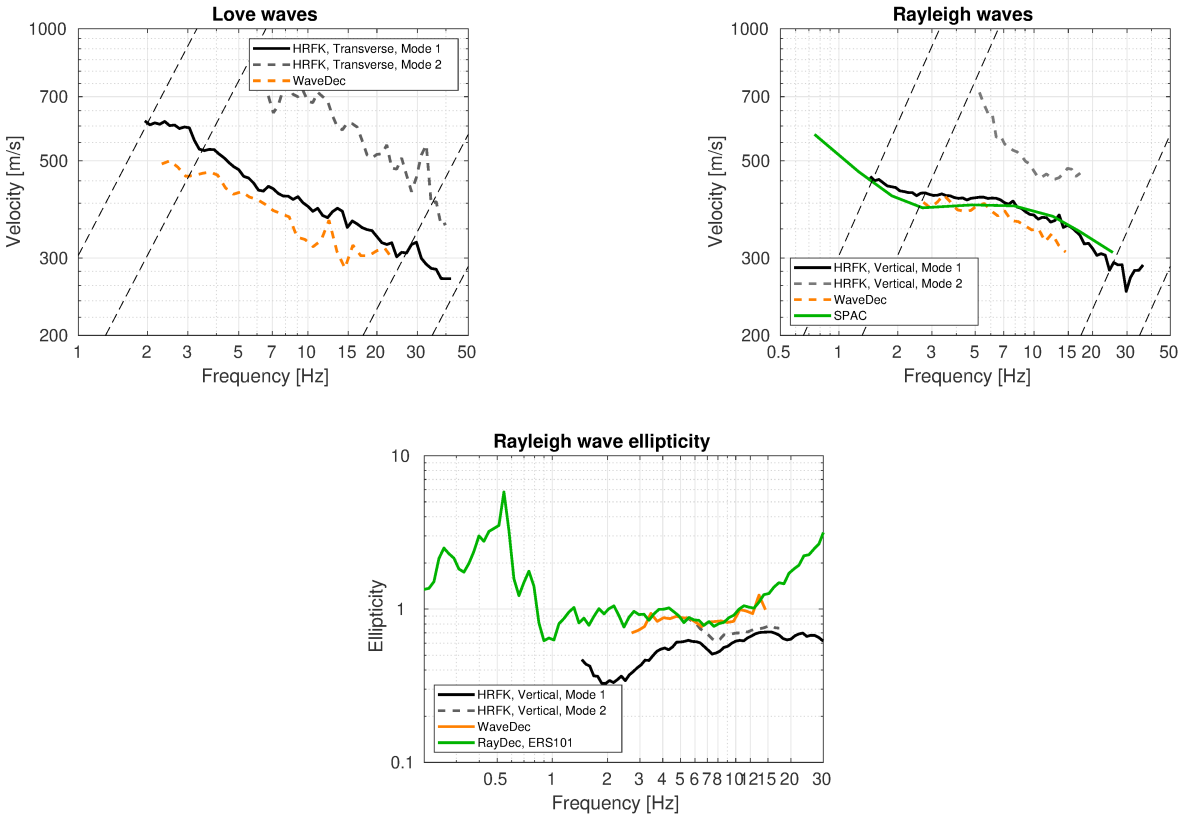

Figure 11: Overview of the Love and Rayleigh wave dispersion curves as well as the ellipticity curves for both arrays. The dashed lines indicate the theoretical resolution limits of the array. The RayDec ellipticity curve corresponds to station ERS101.

4 Data inversion

4.1 Inversion targets

As the measured ellipticity curves contain the 2-dimensional resonance effects of the valley, we did not use them for the inversion. For Rayleigh waves, the fundamental mode as identified by HRFK was used as inversion target. For Love waves, the two different dispersion curves determined by HRFK and WaveDec have been tested as inversion targets. As it was not possible to fit the HRFK curve together with the Rayleigh wave dispersion curve, especially in the low-frequency part, the Love wave dispersion curve determined by WaveDec was used.
The details of the inversion targets are indicated in Table 1 and the corresponding curves are shown in Fig. 12.

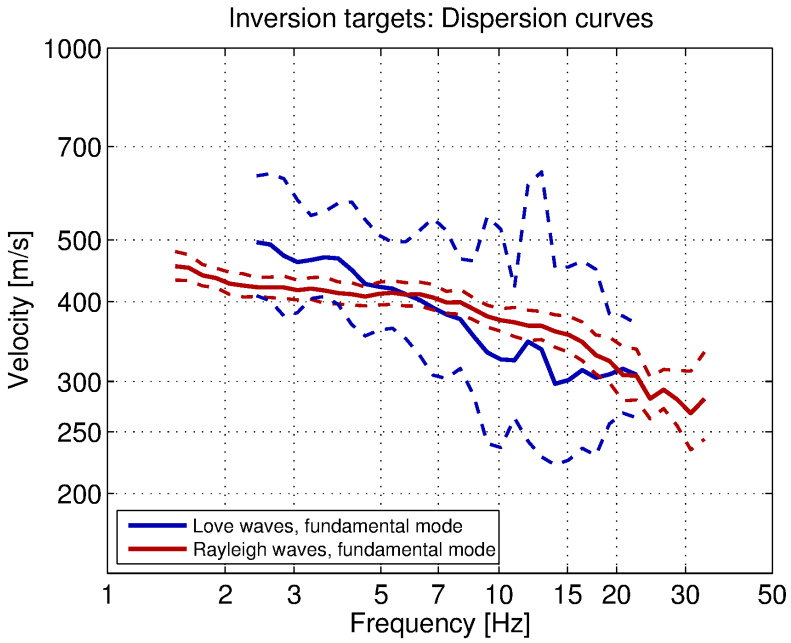

Figure 12: Overview of the dispersion curves used as targets for the different inversions.

Table 1: List of the data curves used as target in the inversion.

Method	Wave type	Mode	Curve type	Frequency range [Hz]
WaveDec	Love	fundamental	dispersion	2.4 - 22.5
HRFK (V)	Rayleigh	fundamental	dispersion	1.5 - 33.5

4.2 Inversion parameterization

For the inversion, seven different parameterizations have been used in total. The first six had free values of the depths and velocities of the different layers, ranging from three to eight layers (including half-space). The last parameterization had fixed layer depths and consisted of 16 layers in total, with the deepest interface at 100 m depth. S- and P-wave velocities were allowed to range from 50 to 3500 m/s and from 100 to 5000 m/s, respectively. The deepest layers were allowed to range to a depth of 100 m for the first six parameterizations. The density was fixed to 2 300 kg/m^3 for the lowest layer and to 2 000 kg/m^3 for all other layers.
Parameterizations allowing low-velocity zones close to the surface have been tested, but these models did not result in a better fit of the dispersion curves. Therefore, only models with increasing S- and P-wave velocity with depth are included in this report.

4.3 Inversion results

We performed a total of seven inversions with different parameterizations (see Table 2). Each inversion run produced 200 000 models in total in order to assure a good convergence of the solution. The results of these inversions are shown in Figs 13 - 19.
All inversions fit the Rayleigh wave dispersion curve in a good way. The fitting of the Love wave dispersion curves is better for the inversions using between four and eight layers. The three-layer and the fixed-depth inversions have a worse fit of the Love wave dispersion curve, resulting in slightly higher misfit values. For the three-layer case, this is certainly caused by the missing complexity of the model. In the fixed-layer case, this can be caused by the inflexibility of the layer depths or a missing conversion of the inversion.

Table 2: List of inversions

Inversion	Number of layers	Number of models	Minimum misfit
SEFS3l	3	200 000	0.311
SEFS4l	4	200 000	0.269
SEFS5l	5	200 000	0.269
SEFS6l	6	200 000	0.269
SEFS7l	7	200 000	0.276
SEFS8l	8	200 000	0.280
SEFSfix	16	200 000	0.310

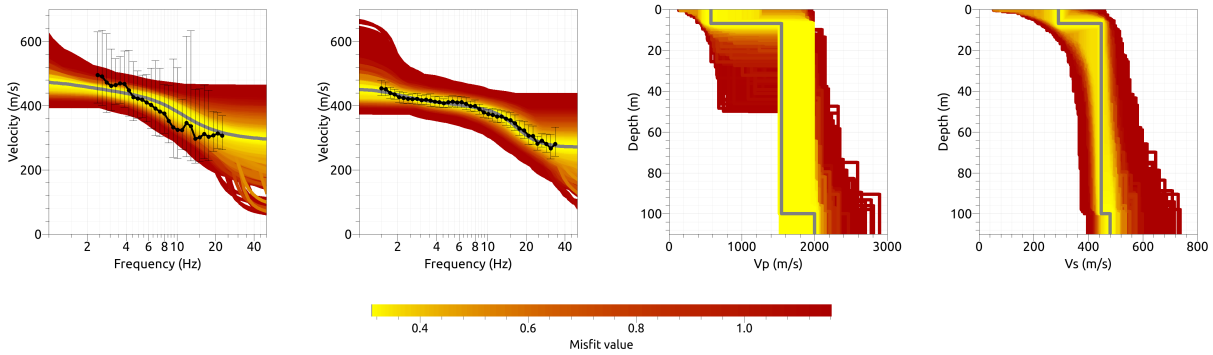

Figure 13: Inversion SEFS3l. From left to right: Dispersion curves for the Love wave fundamental mode and the Rayleigh wave fundamental mode. P-wave velocity profiles and S-wave velocity profiles. The black dots indicate the data points used for the inversion, the gray line indicates the best-fitting model.

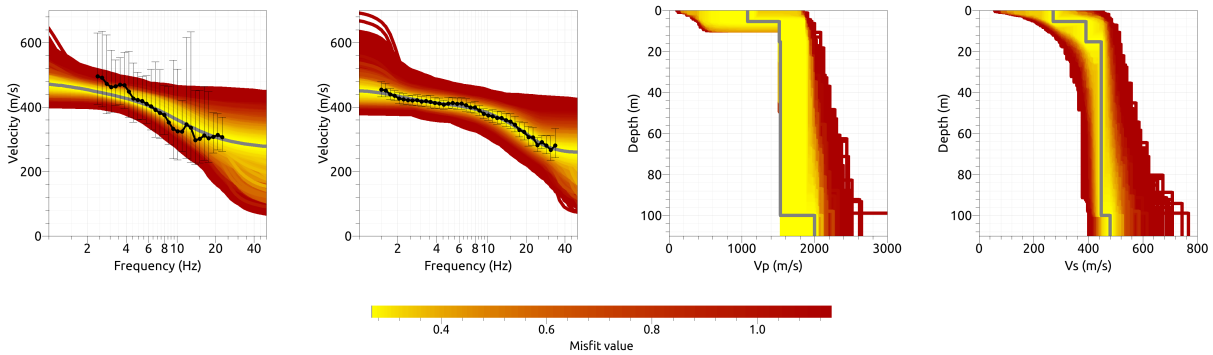

Figure 14: Inversion SEFS4l. From left to right: Dispersion curves for the Love wave fundamental mode and the Rayleigh wave fundamental mode. P-wave velocity profiles and S-wave velocity profiles. The black dots indicate the data points used for the inversion, the gray line indicates the best-fitting model.

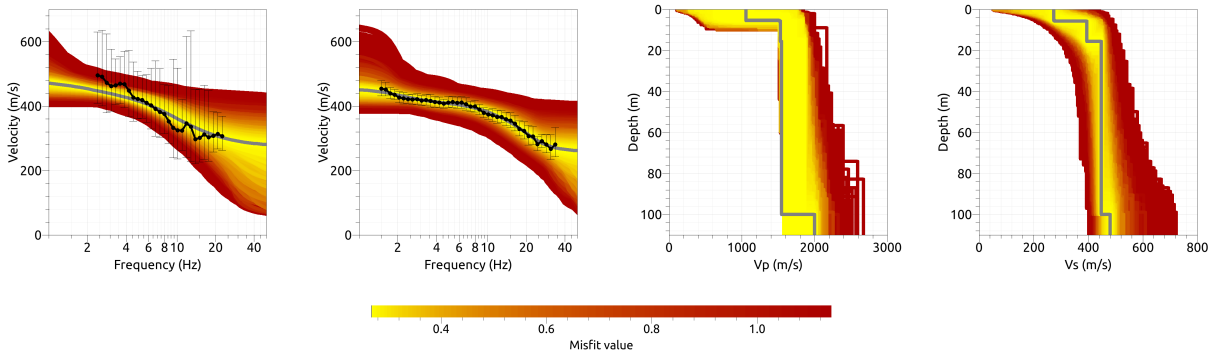

Figure 15: Inversion SEFS5l. From left to right: Dispersion curves for the Love wave fundamental mode and the Rayleigh wave fundamental mode. P-wave velocity profiles and S-wave velocity profiles. The black dots indicate the data points used for the inversion, the gray line indicates the best-fitting model.

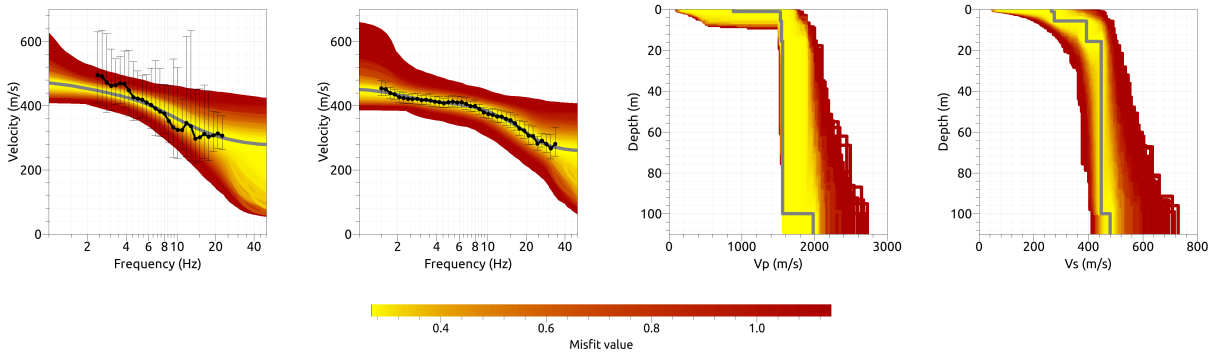

Figure 16: Inversion SEFS6l. From left to right: Dispersion curves for the Love wave fundamental mode and the Rayleigh wave fundamental mode. P-wave velocity profiles and S-wave velocity profiles. The black dots indicate the data points used for the inversion, the gray line indicates the best-fitting model.

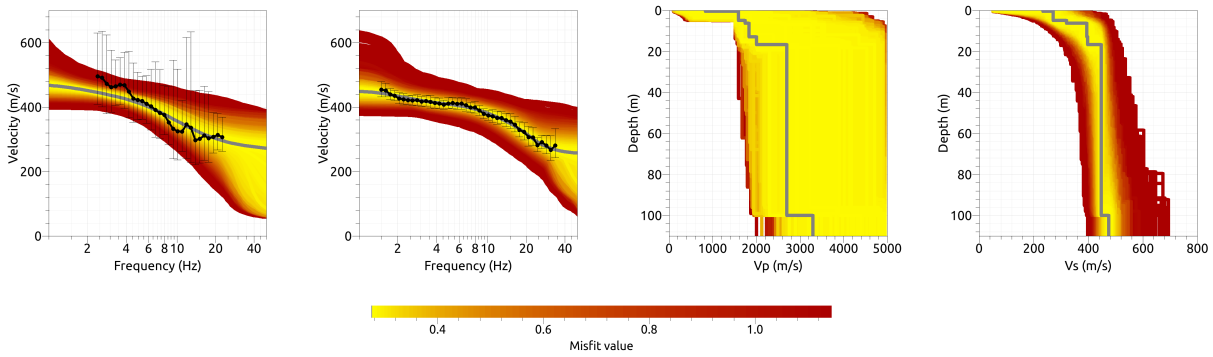

Figure 17: Inversion SEFS7l. From left to right: Dispersion curves for the Love wave fundamental mode and the Rayleigh wave fundamental mode. P-wave velocity profiles and S-wave velocity profiles. The black dots indicate the data points used for the inversion, the gray line indicates the best-fitting model.

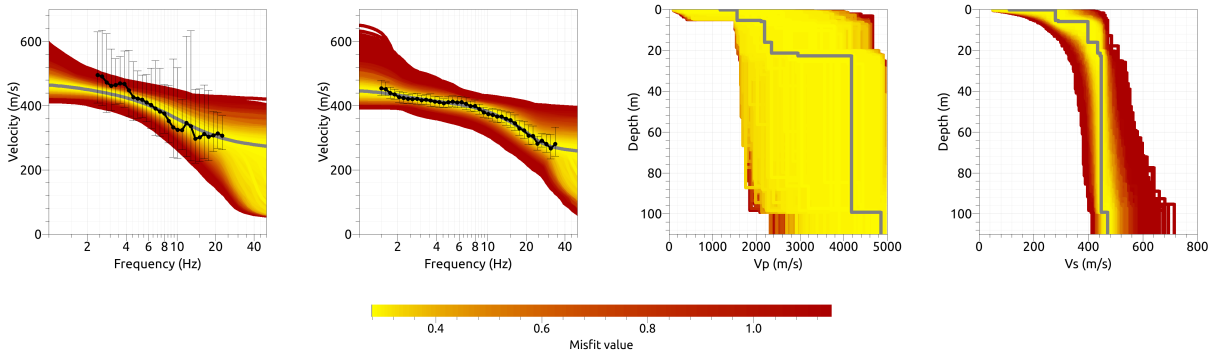

Figure 18: Inversion SEFS8l. From left to right: Dispersion curves for the Love wave fundamental mode and the Rayleigh wave fundamental mode. P-wave velocity profiles and S-wave velocity profiles. The black dots indicate the data points used for the inversion, the gray line indicates the best-fitting model.

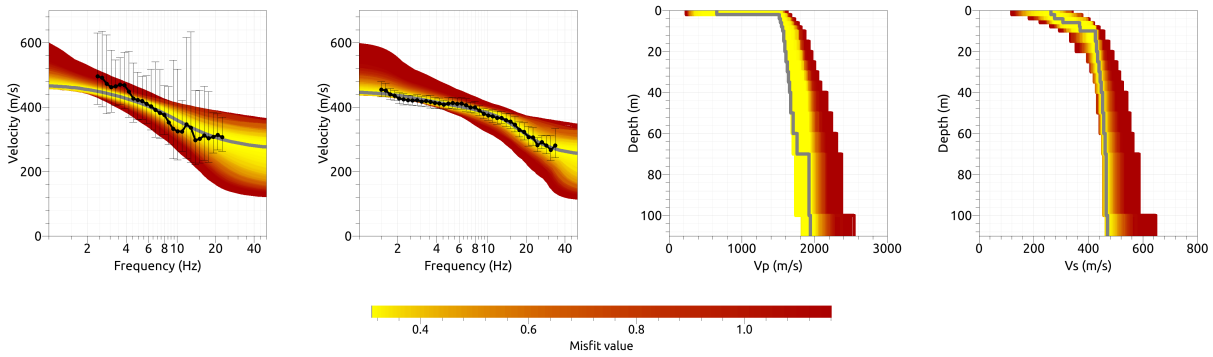

Figure 19: Inversion SEFSfix. From left to right: Dispersion curves for the Love wave fundamental mode and the Rayleigh wave fundamental mode. P-wave velocity profiles and S-wave velocity profiles. The black dots indicate the data points used for the inversion, the gray line indicates the best-fitting model.

4.4 Overview of the inversion result

The best-fitting models of the inversions are shown in Fig. 20. The velocity profiles for the inversions using four to eight layers are very similar. The common features are shear-wave velocities of about 275 m/s in the upper 6 m, followed by a layer with about 395 m/s down to about 16 m. The next layer consistently shows an S-wave velocity of about 448 m/s and goes down to 100 m, where the velocity slightly increases, but stays below 500 m/s. In any case, the measurements only constrain the structure in a reasonable way to a depth of about 75 m (see Fig. 22). Therefore, the deepest interface was not allowed to go deeper than 100 m in the inversion. We cannot resolve the depth of the sedimentary basin and the velocity contrast with the bedrock.
The model using only three layers does not have enough parameters to follow exactly the trend of the other inversions. For the structure below 16 m, it is equivalent with the other models. In the upper part it differs, having a first layer of 290 m/s down to about 7 m, where the layer with 448 m/s directly follows.
The best model for the inversion with the fixed depths is, as expected, smoother than the other models. It also shows an intermediate velocity contrast at 10 m depth and the velocities below gradually increase from 426 to 471 m/s between 10 and 100 m of depth.
The three-layer model has a V_{S30} of 398.6 m/s, all other inversions give models with V_{S30} between 378.5 and 385.0 m/s, with an average value of $382.8 \pm 2.4\, m/s$. All models except the three-layer model will be accepted results of the inversion.

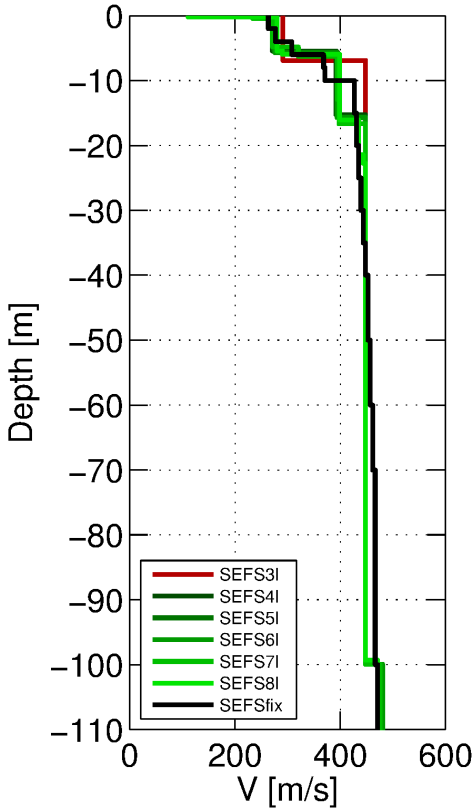

Figure 20: Overview of the shear-wave velocity profiles of the the different inversions.

4.5 SH transfer function

In Fig. 21, the average theoretical shear-wave transfer function for the models resulting from the inversions are shown. As these models did not resolve the velocity contrast to the bedrock, the transfer function is rather flat and oscillates around 2.5. Unfortunately, we do not have empirical amplification functions to compare the data so far. In any case, we expect the 2-dimensional resonance effects of the valley to be reflected in the empirical amplification. In Fig. 21, we also modeled the effect of a strong velocity contrast on the amplification functions by adding a layer with S-wave velocity of 2000 m/s at a depth of 150 m and 300 m. We can see that in this case, the amplification at some frequencies is much larger. In any case, the 2-dimensional resonance of the valley will influence the amplification of seismic waves and we expect the empirical amplification to show peak at the respective frequencies of the 2-dimensional resonances of the valley. Modeling the interface at different depths than 150 or 300 m results in a curve which is stretched with respect to those for the 150 and 300 m cases.

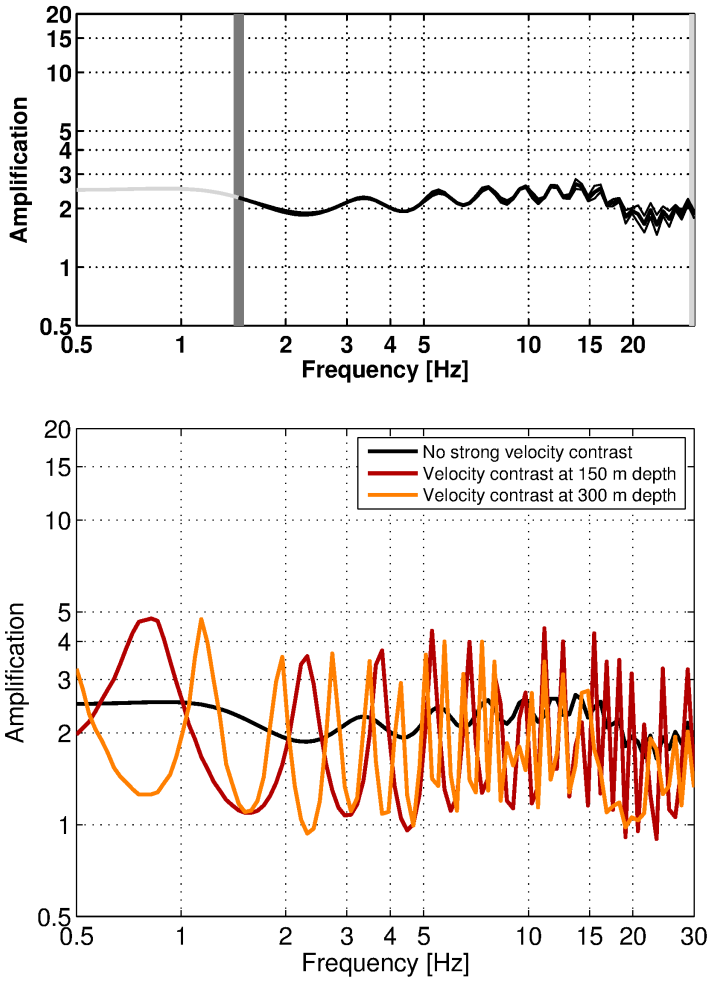

Figure 21: Top: Modeled amplification for the best models of the six inversions with at least four layers (black, with standard deviation). The vertical dark grey bar indicates the lowest frequency of the dispersion curves used in the inversion. Bottom: Comparison of the modeled amplification for the models resulting from the inversion with models obtained after adding a velocity contrast ($V_S = 2000\,m/s$) at a depth of 150 m or 300 m.

4.6 Quarter-wavelength representation

The quarter-wavelength velocity approach (Joyner et al., 1981) provides, for a given frequency, the average velocity at a depth corresponding to 1/4 of the wavelength of interest. It is useful to identify the frequency limits of the experimental data (the minimum frequency of the dispersion curve used in the inversion is 1.5 Hz). The results using this proxy show that the dispersion curves constrain the profiles down to about 75 m (Fig. 22). Moreover, the quarter wavelength impedance-contrast introduced by Poggi et al. (2012) is also displayed in the figure. It corresponds to the ratio between two quarter-wavelength average velocities, respectively from the top and the bottom part of the velocity profile, at a given frequency (Poggi et al., 2012). As the velocity profiles do not include strong velocity contrasts, this curve is rather flat.

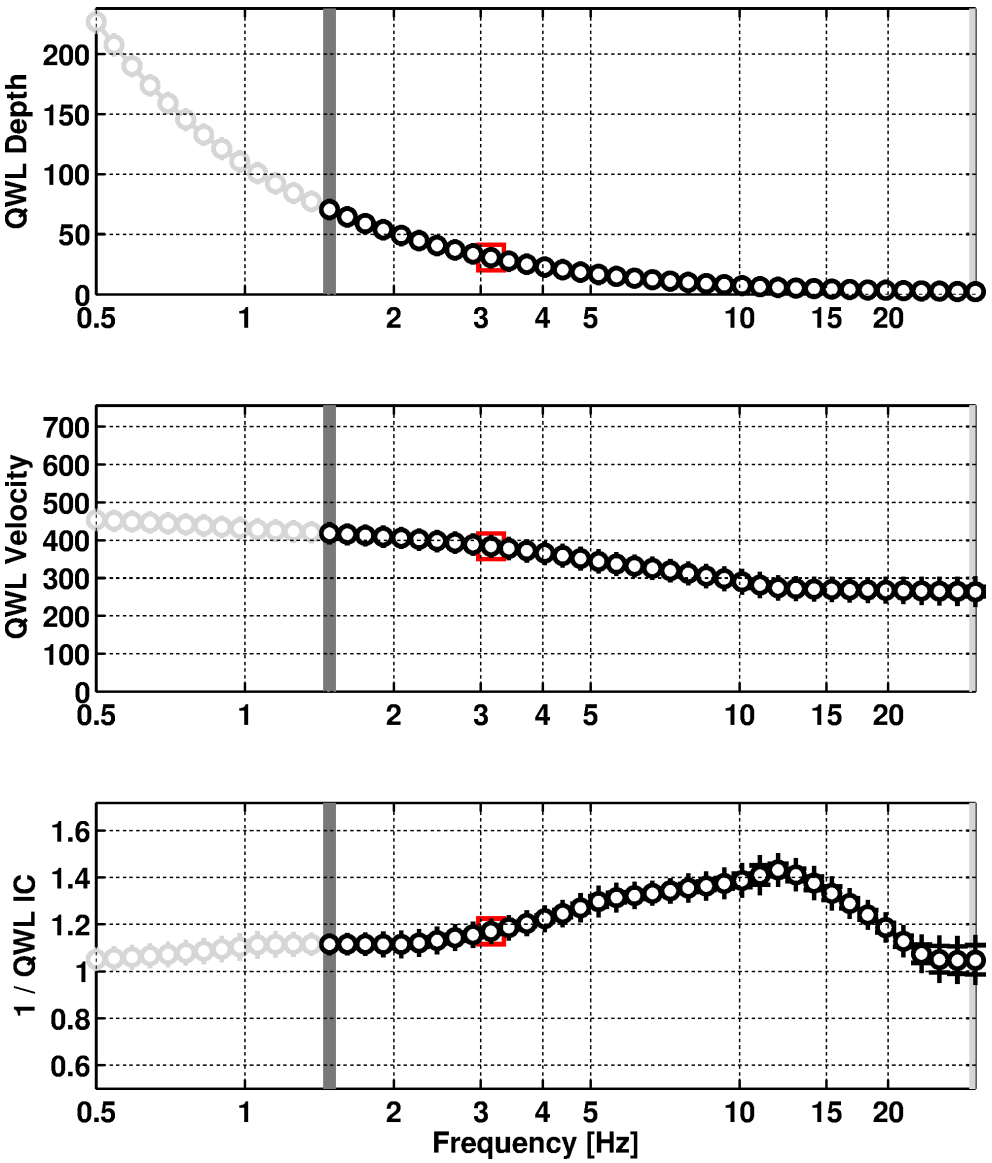

Figure 22: Quarter wavelength representation of the velocity profile for the best models of the inversions (top: depth, center: velocity, bottom: inverse of the impedance contrast). The black curves are constrained by the dispersion curves, the light grey curves are not constrained by the data. The red square corresponds to V_{S30}.

5 2-dimensional polarization effects

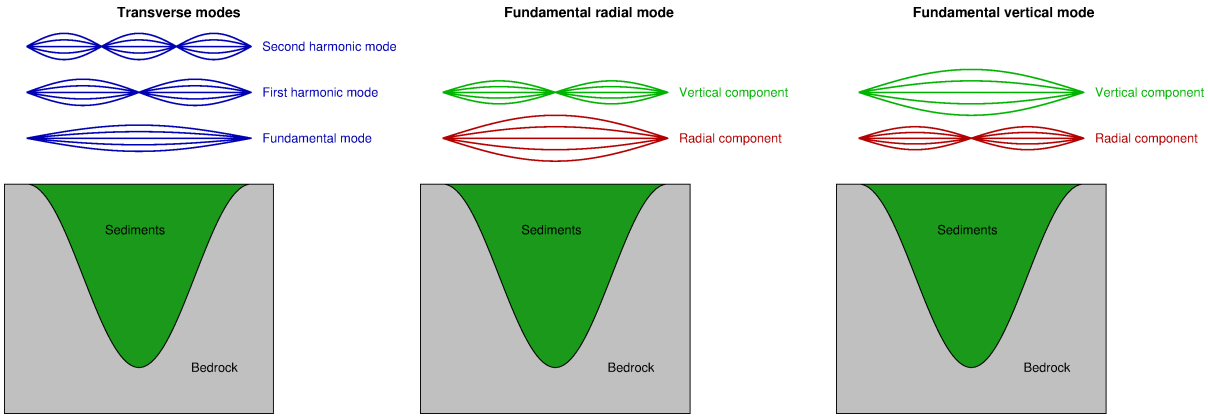

Figure 23: Sketch of the different modes of the eigenvibrations for a simple valley with a cosine-shaped sedimentary filling.

The inversion of the measured dispersion curves does not allow us to constrain the depth of the bedrock at the site. A more detailed investigation of the eigenmodes of the valley resonances could help us to resolve the deeper structure. Fig. 23 gives an overview of the theoretical shapes of the different modes of a simple valley where the cross-section of the sedimentary filling is cosine-shaped. The transverse modes are only visible on the transverse components of the valley, i.e. move along the valley axis. The fundamental transverse mode has a node on the basin borders and a maximum amplitude at the valley center. The first harmonic mode will have an additional node in the valley center and the two parts of the movement will be in opposite phase. The second harmonic mode will have two nodes inside the valley and the two outermost parts of the valley will move in phase, while the central part will move in opposite phase.
The radial and vertical modes are coupled, i.e. their movement is visible on both the radial and the vertical component. The fundamental radial mode corresponds to a movement where one half of the valley is moving upwards, while the other half is moving downwards and vice versa. In the same time, the horizontal motion is maximum in the valley center. The fundamental vertical mode finally corresponds to a "breathing" of the valley, i.e. the valley is increasing and decreasing its volume. The corresponding particle motion is maximum in the center for the vertical motion, while it is zero at the center and in opposite phase for the two halves of the valley on the radial component. The higher modes of the radial and vertical modes are more complex.

Bard and Bouchon (1985) give the following formula for the different modes of the transverse (or SH) resonance of a valley:

$$f^T_{mn} = \frac{v_S}{4h}\sqrt{(2m+1)^2 + (n+1)^2 \cdot \left(\frac{2h}{l}\right)^2}, \tag{1}$$

where v_S is the average shear-wave velocity in the sediments, h the maximum thickness of the sediments and l the half-width of the sedimentary basin, i.e. the width over which the sedimentary filling is more than half of the maximum thickness deep. m indicates the number of vertical nodes (and is 0 in the examples of Fig. 23), n the number of horizontal

nodes. We will assume $m = 0$ in the following.
For the radial and vertical resonance modes, the theoretical frequencies cannot be calculated analytically and Bard and Bouchon (1985) give these approximate formulas for the respective fundamental modes:

$$f_0^R = \frac{v_S}{4h}\sqrt{1 + \left(\frac{2.9h}{l}\right)^2}, \tag{2}$$

$$f_0^V = \frac{v_P}{4h}\sqrt{1 + \left(\frac{h}{l}\right)^2}. \tag{3}$$

For the vertical resonance frequency, the P-wave velocity is used instead of the S-wave velocity.

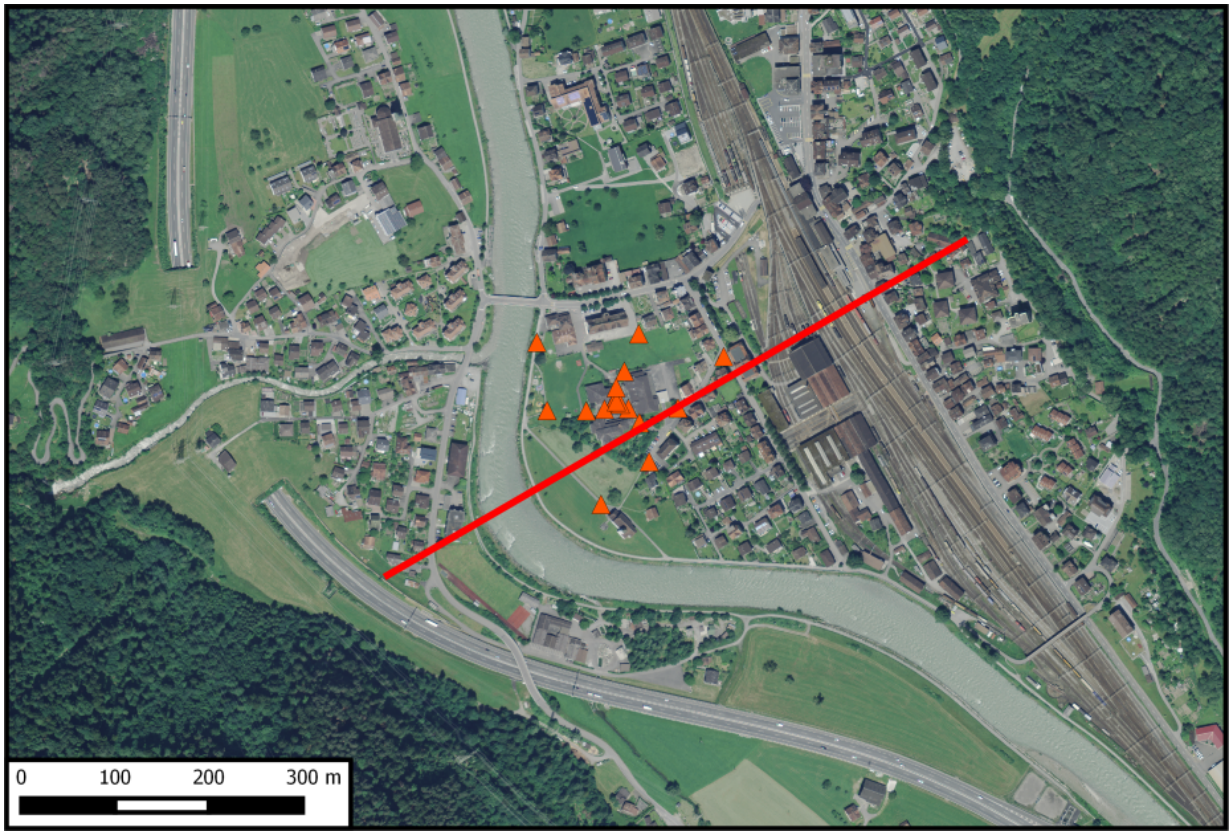

Figure 24: Profile across the valley on which the different sensor singals have been projected. The profile has a length of about 720 m.

In order to analyze the different modes, we have to rotate the components of the different sensors in order to separate the radial and transverse components. In the case of Erstfeld, the valley axis follows the direction 150°/330° (see profile in Fig. 24). We rotate the signals of all sensor in this direction and get the spectra shown in Fig. 25.

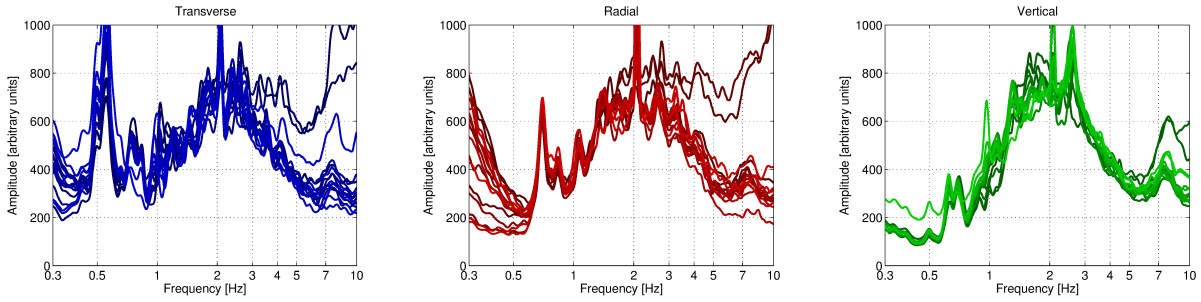

Figure 25: Spectral amplitudes for all array stations after rotation. The transverse component is oriented along the valley axis, the radial component perpendicular to the valley axis.

On the transverse component, we can clearly identify peaks at 0.559 Hz and 0.741 Hz (and 1.054 Hz), respectively. On the radial component, we see several peaks at 0.696 Hz, 0.840 Hz and 1.054 Hz, and on the vertical component, we can identify peaks at 0.628 Hz and 0.696 Hz. We project all array stations on a line across the valley (see Fig. 24). The respective amplitudes at these frequencies are shown in Fig. 26. We do not know the shape of the sedimentary cover along the profile. It has a maximum width of about 720 m. The stations of the array cover only one half of the valley, the easternmost station is located at the approximate center of the array. Therefore, we cannot observe the full shape of the respective modes.
The observed amplitudes at 0.559 Hz show an increasing trend towards the valley center, which is compatible with the theoretical shape of the fundamental transverse mode. At 0.628 Hz, there is no clear trend visible. At 0.696 Hz, the radial component shows an increasing amplitude trend towards the valley center, the vertical component shows a decreasing trend. This is compatible with the fundamental radial mode. At 0.741 Hz, the transverse component shows a decreasing trend towards the valley center, which is compatible with the first harmonic transverse mode. At 0.840 Hz, both the radial and vertical components are increasing towards the valley center. The mode attribution remains unclear. The amplitudes at 1.054 Hz are relatively stable for the radial and vertical component, but the transverse component is first decreasing and then increasing again along the profile. This might actually be the second harmonic transverse mode.
For a clearer identification of the eigenmodes, it would be necessary to measure them along the full profile of the valley.

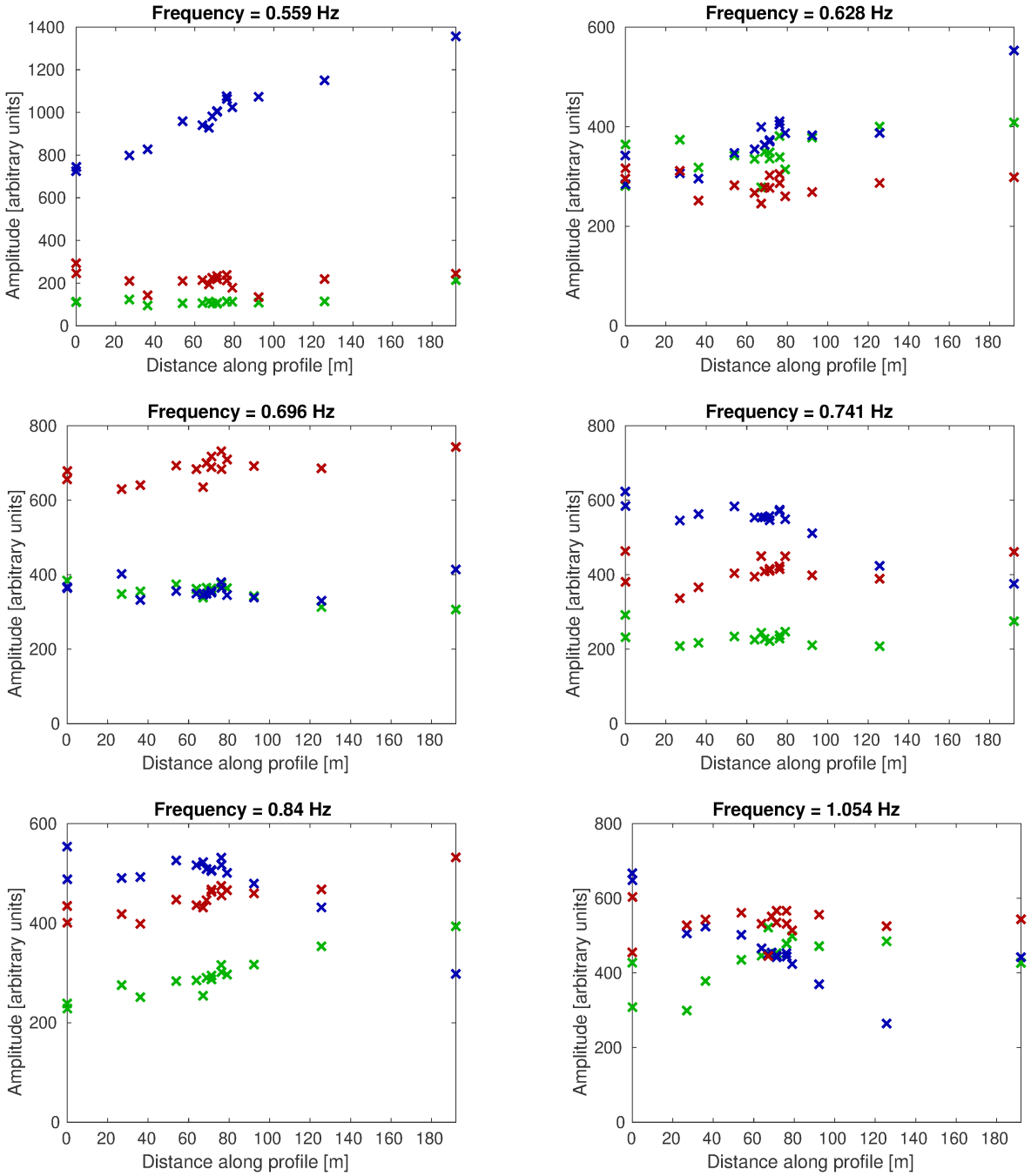

Figure 26: Spectral amplitudes for some peak frequencies for all array stations after rotation and projection along a line across the valley. The length along the profile is indicated as a distance from the westernmost station. The blue, red and green colors correspond to the transverse, radial and vertical components, respectively.

6 Conclusion

We performed a passive array measurement to characterize the soil underneath station SEFS in Erstfeld (UR), located on an alluvial deposits in the Reuss valley.
The dispersion curves for Love and Rayleigh waves could be measured over a wide frequency range. The Love wave dispersion curve was measured between 2.4 and 22.5 Hz (fundamental mode), a higher modes could also be identified. For the Rayleigh waves, the fundamental mode dispersion curve was retrieved between 1.5 and 33.5 Hz, and also a higher mode was visible. The stations show a clear H/V peak, which is related with a 2-dimensional resonance effect of the valley. Therefore, no H/V or ellipticity information was used in the inversion for the soil structure.
The joint inversion of Love and Rayleigh wave dispersion curves showed that the structure can be explained by models with at least four layers, and can be simplified by a first layer with a thickness of 6 m and an S-wave velocity of about 275 m/s, followed by a layer with a velocity of 395 m/s down to about 16 m, where the velocity increases to about 448 m/s. The bedrock cannot be retrieved. The V_{S30} of the best models is about 383 m/s, corresponding to soil class B in EC8 and C in SIA261.
Using the array recordings, we can identify the fundamental mode of the valley resonance at about 0.56 Hz and can also find other modes. For a more thorough determination of the eigenmodes in the valley, a more detailed measurement along a profile crossing the whole valley would need to be performed.

Acknowledgements

The authors thank Dario Chieppa and Simon Rouwendaal for their help during the array measurements.

References

Aki, K. (1957). Space and time spectra of stationary stochastic waves, with special reference to microtremors. *Bull. Earthquake Res. Inst. Tokyo Univ.*, 35:415–456.

Bard, P.-Y. and Bouchon, M. (1985). The two-dimensional resonance of sediment-filled valleys. *Bull. Seismol. Soc. Am.*, 75:519–541.

Bettig, B., Bard, P.-Y., Scherbaum, F., Riepl, J., Cotton, F., Cornou, C., and Hatzfeld, D. (2001). Analysis of dense array noise measurements using the modified spatial auto-correlation method (SPAC): application to the Grenoble area. *Boll. Geof. Teor. Appl.*, 42:281–304.

Burjánek, J., Gassner-Stamm, G., Poggi, V., Moore, J. R., and Fäh, D. (2010). Ambient vibration analysis of an unstable mountain slope. *Geophys. J. Int.*, 180:820–828.

Burjánek, J., Moore, J. R., Molina, F. X. Y., and Fäh, D. (2012). Instrumental evidence of normal mode rock slope vibration. *Geophys. J. Int.*, 188:559–569.

Fäh, D., Wathelet, M., Kristekova, M., Havenith, H., Endrun, B., Stamm, G., Poggi, V., Burjanek, J., and Cornou, C. (2009). Using ellipticity information for site characterisation. NERIES deliverable JRA4 D4, available at http://www.neries-eu.org.

Hobiger, M., Bard, P.-Y., Cornou, C., and Le Bihan, N. (2009). Single station determination of Rayleigh wave ellipticity by using the random decrement technique (RayDec). *Geophys. Res. Lett.*, 36.

Joyner, W. B., Warrick, R. E., and Fumal, T. E. (1981). The effect of Quaternary alluvium on strong ground motion in the Coyote Lake, California, earthquake of 1979. *Bull. Seismol. Soc. Am.*, 71(4):1333–1349.

Maranò, S., Reller, C., Loeliger, H.-A., and Fäh, D. (2012). Seismic waves estimation and wavefield decomposition: Application to ambient vibrations. *Geophys. J. Int.*, 191:175–188.

Poggi, V., Edwards, B., and Fäh, D. (2012). Characterizing the Vertical-to-Horizontal ratio of ground motion at soft-sediment sites. *Bull. Seismol. Soc. Am.*, 102(6):2741–2756.

Poggi, V. and Fäh, D. (2010). Estimating Rayleigh wave particle motion from three-component array analysis of ambient vibrations. *Geophys. J. Int.*, 180:251–267.